UNIVERSITY OF AMSTERDAM

UvA-DARE (Digital Academic Repository)

Measuring the Hubble constant with dark neutron star--black hole mergers

Shiralilou, B.; Raaiijmakers, G.; Duboeuf, B.; Nissanke, S.; Foucart, F.; Hinderer, T.; Williamson, A.R.

DOI
10.3847/1538-4357/acf3dc

Publication date
2023

Document Version
Final published version

Published in
Astrophysical Journal

License
CC BY

Link to publication

Citation for published version (APA):
Shiralilou, B., Raaiijmakers, G., Duboeuf, B., Nissanke, S., Foucart, F., Hinderer, T., & Williamson, A. R. (2023). Measuring the Hubble constant with dark neutron star--black hole mergers. *Astrophysical Journal*, *955*(2), Article 149. https://doi.org/10.3847/1538-4357/acf3dc

General rights
It is not permitted to download or to forward/distribute the text or part of it without the consent of the author(s) and/or copyright holder(s), other than for strictly personal, individual use, unless the work is under an open content license (like Creative Commons).

Disclaimer/Complaints regulations
If you believe that digital publication of certain material infringes any of your rights or (privacy) interests, please let the Library know, stating your reasons. In case of a legitimate complaint, the Library will make the material inaccessible and/or remove it from the website. Please Ask the Library: https://uba.uva.nl/en/contact, or a letter to: Library of the University of Amsterdam, Secretariat, Singel 425, 1012 WP Amsterdam, The Netherlands. You will be contacted as soon as possible.

UvA-DARE is a service provided by the library of the University of Amsterdam (https://dare.uva.nl)

Download date:24 Jan 2024

The Astrophysical Journal, 955:149 (11pp), 2023 October 1 https://doi.org/10.3847/1538-4357/acf3dc
© 2023. The Author(s). Published by the American Astronomical Society.
OPEN ACCESS

Measuring the Hubble Constant with Dark Neutron Star–Black Hole Mergers

Banafsheh Shiralilou[1], Geert Raaiijmakers[1], Bastien Duboeuf[2], Samaya Nissanke[1,3], Francois Foucart[4], Tanja Hinderer[5], and Andrew R. Williamson[6]

[1] GRAPPA, Anton Pannekoek Institute for Astronomy and Institute of High-Energy Physics, University of Amsterdam, Science Park 904, 1098 XH Amsterdam, The Netherlands
[2] University of Lyon, ENS de Lyon, CNRS, Laboratoire de Physique, F-69342, Lyon, France
[3] Nikhef, Science Park 105, 1098 XG Amsterdam, The Netherlands
[4] Department of Physics & Astronomy, University of New Hampshire, 9 Library Way, Durham, NH 03824, USA
[5] Institute for Theoretical Physics, Utrecht University, Princetonplein 5, 3584 CC, Utrecht, The Netherlands
[6] University of Portsmouth, Portsmouth, PO1 3FX, UK

Received 2022 August 2; revised 2023 August 21; accepted 2023 August 23; published 2023 September 28

Abstract

Detection of gravitational waves (GWs) from neutron star-black hole (NSBH) standard sirens provides local measurements of the Hubble constant (H_0), regardless of the detection of an electromagnetic (EM) counterpart, given that matter effects can be exploited to break the redshift degeneracy of the GW waveforms. The distinctive merger morphology and the high-redshift detectability of tidally disrupted NSBH make them promising candidates for this method. Also, the detection prospects of an EM counterpart for these systems will be limited to $z < 0.8$ in the optical, in the era of future GW detectors. Using recent constraints on the equation of state of NSs from multi-messenger observations of NICER and LIGO/Virgo/KAGRA, we show the prospects of measuring H_0 solely from GW observation of NSBH systems, achievable by the Einstein telescope (ET) and Cosmic Explorer (CE) detectors. We first analyze individual events to quantify the effect of high-frequency ($\geqslant$500 Hz) tidal distortions on the inference of NS tidal deformability parameter (Λ) and hence on H_0. We find that disruptive mergers can constrain Λ up to $\mathcal{O}(60\%)$ more precisely than nondisruptive ones. However, this precision is not sufficient to place stringent constraints on the H_0 from individual events. By performing Bayesian analysis on simulated NSBH data (up to $N = 100$ events, corresponding to a day of observation) in the ET+CE detectors, we find that NSBH systems enable unbiased 4%–13% precision on the estimate of H_0 (68% credible interval). This is a similar measurement precision found in studies analyzing NSBH mergers with EM counterparts in the LVKC O5 era.

Unified Astronomy Thesaurus concepts: Cosmology (343); Gravitational waves (678); General relativity (641); Gravitational wave sources (677); Gravitational wave astronomy (675)

1. Introduction

The value of the Hubble constant H_0, which quantifies the current expansion rate of the Universe, has been measured extensively since it was first established in 1929 (Hubble 1929). Even with the current high-precision measurements of H_0, the most recent local measurement $H_0 = 73.04 \pm 1.04$ km s^{-1} Mpc^{-1} of the Hubble Space Telescope and Supernova H0 for the Equation of State (SH0eS) team (Riess et al. 2021), highlights a level of $\approx 5\sigma$ tension with the constraint inferred by the Planck Collaboration, $H_0 = 67.4 \pm 0.5$ km s^{-1}Mpc^{-1} (Planck Collaboration et al. 2020). Despite the ongoing efforts to find conclusive evidence of systematic errors in modeling the data of these experiments, or a compelling novel theoretical explanation, there is currently no agreement on the cause of the discrepancy in H_0 between the different measurements.

Gravitational wave (GW) detection and sky localization of merging binaries can provide a direct and independent local measurement of H_0, as first proposed by Schutz (1986), and further analyzed and advanced by Holz & Hughes (2005), Dalal et al. (2006), Nissanke et al. (2010, 2013a), Taylor et al. (2012), Oguri (2016), Seto & Kyutoku (2018), Chen et al. (2018), Vitale & Chen (2018), Fishbach et al. (2019), Feeney et al. (2019), Mortlock et al. (2019), Soares-Santos et al. (2019), Palmese et al. (2020), Vasylyev & Filippenko (2020), Chen et al. (2022), Gayathri et al. (2020), Borhanian et al. (2020), Mukherjee et al. (2020, 2021b), Feeney et al. (2021), Gray et al. (2022), and Cigarrán Díaz & Mukherjee (2022). These systems are referred to as bright standard sirens, in case an EM follow-up can be assigned to the event, and otherwise dark standard sirens. The GW detection of the binary neutron star (BNS) system GW170817 and the electromagnetic (EM) identification of its host galaxy (Abbott et al. 2017a, and references therein) allowed the first application of the bright standard siren's approach, giving $H_0 = 70^{+12.0}_{-8.0}$ km s^{-1} Mpc^{-1} (Abbott et al. 2017b). This measurement was followed by an improved estimate of $H_0 = 68.9 \pm 4.7$ km s^{-1} Mpc^{-1} (Hotokezaka et al. 2019), using high angular resolution imaging of radio counterparts of GW170817, and later on estimated to $H_0 = 68.3^{+4.6}_{-4.5}$ km s^{-1} Mpc^{-1} Mukherjee et al. (2021a) and $H_0 = 68.6^{+14.0}_{-8.5}$ km s^{-1} Mpc^{-1} (Nicolaou et al. 2020), by accounting for the systematic uncertainties that arise from the calculation of the peculiar velocity. Recently, the third GW catalog was released, bringing the total number of GW detections to 90 events (LIGO Scientific Collaboration et al. 2021). Selecting 47 of these events, the Hubble constant was constrained to $H_0 = 68^{+13.0}_{-7.0}$ km s^{-1} Mpc^{-1} when using the redshifted mass distribution, and $H_0 = 68^{+8.0}_{-6.0}$ km s^{-1} Mpc^{-1} when combining the GW information with a galaxy catalog

Original content from this work may be used under the terms of the Creative Commons Attribution 4.0 licence. Any further distribution of this work must maintain attribution to the author(s) and the title of the work, journal citation and DOI.

(Abbott et al. 2023), and to $H_0 = 67^{+6.3}_{-3.8}$ km s^{-1} Mpc^{-1} when using the GWTC-3 catalog in combination with a galaxy catalog (Mukherjee et al. 2022).

The combined GW and EM detection of NSBH systems, however, has yet to be observed. In general, NSBH systems are expected to be promising standard sirens—as both dark and bright candidates–since they have higher masses compared to BNSs, leading to mergers that occur at lower frequencies, potentially within the current and future ground-based detector bands, and also accessible at higher redshifts (Nissanke et al. 2010; Vitale & Chen 2018; Feeney et al. 2021). The key difference between the NSBH systems and BNSs, which makes NSBH systems specifically interesting, is in their late-inspiral and merger phenomenology: they allow for both disruptive and nondisruptive mergers. Close to the merger of NSBHs, the strong tidal fields of the BH can, in some cases, significantly disrupt the NS, causing a sudden decrease in the GW amplitude at high frequencies and an accelerated merger, followed by mass ejection and formation of accretion torus around the BH and consequently, EM radiation (disruptive merger). The other possible fate of the NS is that it plunges into the BH before getting highly disrupted and having a chance to emit any EM radiation (nondisruptive merger) (Brege et al. 2018; Foucart et al. 2019a, 2019b) (see Foucart 2020 for a brief overview). Whether the disruption happens or not, and how strong it is, depends primarily on the eccentricity, mass, and spin of the BH, and the internal NS matter structure (Lattimer & Schramm 1974; Vallisneri 2000; Etienne et al. 2009; Shibata et al. 2009; Stephens et al. 2011; Foucart 2012; Foucart et al. 2013b; Deaton et al. 2013; Pannarale et al. 2015a).

In the highly disruptive cases that lead to EM radiation, NSBH systems can be used as bright standard sirens (Nissanke et al. 2010; Vitale & Chen 2018; Feeney et al. 2021) with the spectroscopic redshift for the host being obtained with very high accuracy. Identifying such EM counterparts, however, remains challenging as the current and future planned EM facilities have limitations in the sky coverage (Metzger & Berger 2012; Nissanke et al. 2013b; Sathyaprakash et al. 2019; Raaijmakers et al. 2021b; Chase et al. 2022) and hence many of such events will be too far ($z > 1$) to be detectable by wide-field optical and radio telescopes. Moreover, the probability of detecting an EM counterpart could strongly depend on the orientation angle of the system.

In the cases when no EM counterpart is observed or generated, GW measurements of BNS or NSBH mergers can solely constrain the distance–redshift relation (hence the cosmological parameters), with a method first proposed by Messenger & Read (2012) and applied to BNS mergers more recently by Del Pozzo et al. (2017), Chatterjee et al. (2021), and Ghosh et al. (2022) (see Farr et al. 2019 for a technique applicable to BBHs). Tidal deformation in a binary system affects the transfer of GW energy, and consequently, the GW phase and amplitude evolution and also accelerates the coalescence. In the absence of such matter effects, the mass parameters of GW signals are degenerate with the redshift z, resulting in the detection of redshifted masses $m_{\mathrm{NS},d}$ measured by the detector. However, the tidal corrections in the GW signals depend on the physical masses i.e., the source-frame NS masses such that $m_{\mathrm{NS},s} = m_{\mathrm{NS},d}/(1+z)$. Therefore, these tidally dependent corrections break the degeneracies in the waveform and thus allow the simultaneous estimation of the GW luminosity distance d_L and redshift z, from the waveform's amplitude and phase, respectively.

To constrain H_0 with this approach, we need independently derived information on the NS matter effects, either by assuming a known NS equation of state (EoS) (Messenger & Read 2012) or by using some form of parameterization—such as Taylor expansion of Λ in terms of NS mass—in an EoS-insensitive way. An example of the latter is using one of the so-called universal binary-Love relations (Yagi & Yunes 2017; Doneva & Pappas 2018), which fits Λ around a fiducial NS mass value for which the tidal parameter is known. This approach is so far only applied to GW170817 for which the NS has a fiducial mass that lies in the steepest region of the mass–radius plot. Although this approach is applicable to both stiff and soft NS matter effects, the practical limitation comes from keeping a finite number of terms in the Taylor expansion of Λ. Given this, probing the extreme cases and very high NS masses with this approach can be limited.

In this paper, we use a new approach for modeling the viable EoS parameters, which shall bypass such modeling limitations by relying on observational constraints. We use the posterior EoS samples from Raaijmakers et al. (2021a), which are inferred from a combination of multi-messenger astrophysical observations and low-density nuclear calculations done within a chiral effective field theory framework (Hebeler et al. 2013). The astrophysical observations include the two mass–radius measurements of millisecond pulsars PSR J0030+0451 (Miller et al. 2019; Riley et al. 2019) and PSR J0740+6620 (Miller et al. 2021; Riley et al. 2021) by NASA's Neutron Star Interior Composition Explorer (NICER; Gendreau et al. 2016) and the tidal deformability measurement from GW170817 and its accompanying EM counterpart AT2017gfo, as well as the low signal-to-noise ratio (S/N) event GW190425 (see also Guerra Chaves & Hinderer 2019; Dietrich et al. 2020; Pang et al. 2021) for which no EM counterpart was observed.

In addition to the uncertainties in the modeling techniques, the significance with which H_0 can be inferred also depends on how well the tidal deformability parameter Λ can be constrained by the observed GWs. Note that measuring H_0 with this approach is not applicable to the recently detected NSBH systems GW200105 and GW200115 (Abbott et al. 2021) due to the low S/N of their detected signals and the uninformative constraints on their Λ parameter with the current detectors. This itself is partly due to the lack of information from their merger stage and partially due to the fact that given their asymmetric mass ratios they are (very likely) non-disrupting systems and hence uninformative even at high S/Ns.

In this paper, we determine constraints on Λ—and consequently on H_0—by performing Bayesian parameter estimation on simulated NSBH binary systems in the next-generation detectors, ET (Maggiore et al. 2020) + CE detector era (Reitze et al. 2019; Evans et al. 2021), using the aforementioned multi-messenger constraints on NS EoS to model Λ. We compare the bounds on Λ and H_0 derived from the tidally disrupted and non-disrupted mergers to see how the high-frequency NS disruption effects in the waveforms can improve the overall parameter inference in the era of these next-generation observatories. Our primary interest is in the tidally disrupted systems (i.e., systems with low-mass ratios and possibly high prograde BH spins) as most of them can merge inside the ET +CEs detector bandwidth while the current ground-based detectors cannot capture these high-frequency mergers.

In order to model the GW strain data, we use the NSBH-specific GW waveform model `IMRPhenomNSBH` (Thompson

et al. 2020) (hereafter referred to as Phenom-NSBH). We then analyze the prospects of measuring H_0 by performing a two-step Bayesian parameter estimation on simulated individual NSBH systems, as well as catalogs of NSBH events with different numbers of simulated events. We use the same waveform model for both the injection and recovery of the waveforms.

This paper is organized as follows. In Section 2, we introduce our approach for modeling the tidal deformability parameter, and give an overview of the tidal modeling in the chosen waveform approximation. After explaining the details of source and population simulations in Section 2.3, we describe the details of the Bayesian statistical framework used in our analysis in Section 2.4.1. We present the results of analyzing single NSBH systems and stacked catalogs in Section 3. Section 4 summarizes our conclusions.

2. Methods

2.1. Tidal Deformability Model

During the evolution of an NSBH binary, the tidal fields of the BH produce deformations in the companion NS. These deformations depend on the NS matter properties, predominantly through an EoS-dependent dimensionless tidal deformability parameter Λ defined as

$$\Lambda = \frac{2}{3}\frac{k_2}{\mathcal{C}^5} = \frac{2}{3}k_2\left(\frac{c^2 R}{G m_{\mathrm{NS},s}}\right)^5 = \lambda G\left(\frac{c^2(1+z)}{G m_{\mathrm{NS},d}}\right)^5, \quad (1)$$

where $m_{\mathrm{NS},s}$ is the source-frame mass of the NS, $\mathcal{C} = G m_{\mathrm{NS},s}/Rc^2$ is the NS compactness, and k_2 is the dimensionless relativistic quadrupole tidal Love number such that $\lambda = 2/3 R^5 k_2 G^{-1}$ (with R being the NS radius) characterizes the strength of the induced quadrupole given an external tidal field (Flanagan 1998; Hinderer et al. 2010). The right-hand side of the equation shows the redshift dependency once we transform to detector-frame mass $m_{\mathrm{NS},d} = m_{\mathrm{NS},s}(1+z)$.

We base our modeling of the tidal deformability parameter on the EoS constraints inferred by Raaijmakers et al. (2021a) (For other multi-messenger EoS constraints, see, e.g., Dietrich et al. 2020; Al-Mamun et al. 2021; Huth et al. 2022). In this work, the EoS is constrained by employing a parameterized high-density EoS, coupled to low-density NS matter calculations within a chiral effective field theory framework (Hebeler et al. 2013). Posterior distributions on the EoS parameters are then obtained by combining information from NICER's mass and radius measurements of the pulsars PSR J0030+0451 (Miller et al. 2019; Riley et al. 2019) and PSR J0740+6620 (Miller et al. 2021; Riley et al. 2021), and measurements of the tidal deformability from GW170817 (together with its optical counterpart AT2017gfo) and GW190425. Figure 1 shows the mass–radius and mass-tidal deformability constraints as found by the NICER and LIGO/Virgo observations as well as the possible EoS relations consistent with the posterior distribution found in Raaijmakers et al. (2021a).

Instead of sampling Λ, we sample EoSs from the posterior distribution of Raaijmakers et al. (2021a). For a drawn EoS, a value of Λ can then be assigned based on a given $m_{\mathrm{NS},s}$. By considering a broad set of EoSs as a prior in our analysis, we can take into account the uncertainties in the NS's microphysics. However, we remain dependent on our choice of EoS parameterization, which may introduce a systematic bias. We specifically take the results from the piecewise-polytropic parameterization employed in Raaijmakers et al. (2021a), but note that many other high-density parameterizations exist (Lindblom 2018; Greif et al. 2019; Capano et al. 2020; O'Boyle et al. 2020) as well as nonparametric methods (Landry & Essick 2019; Essick et al. 2020; Landry et al. 2020; Legred et al. 2021). Although this approach does not provide an EoS-insensitive model, the advantage of this approach is that it does not require an approximate analytical modeling of the Λ parameter and is based on the current empirical multi-messenger constraints.

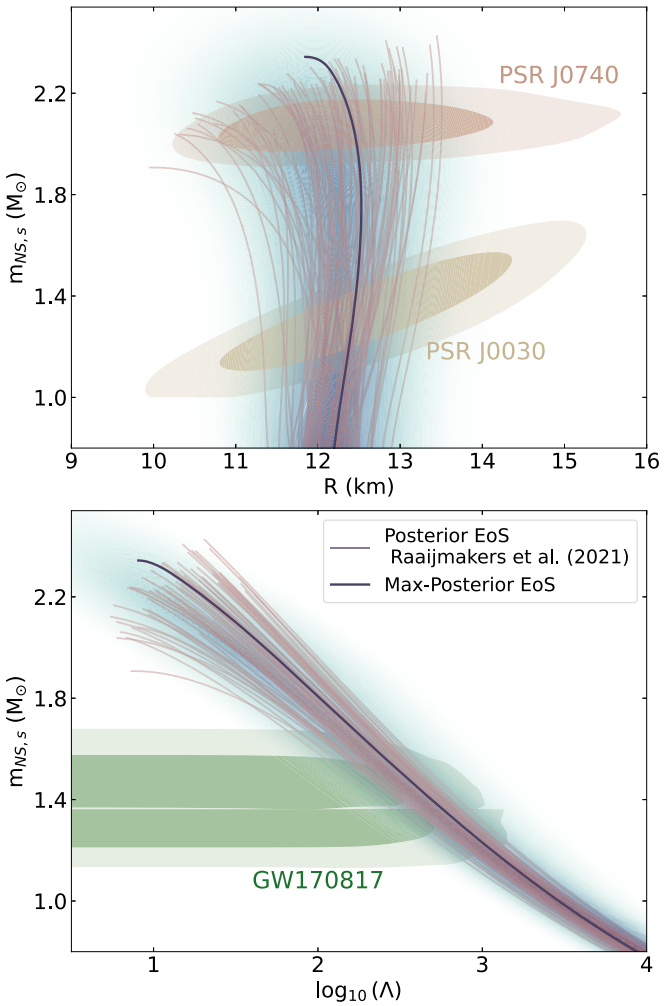

Figure 1. The combined mass–radius constraints found by LIGO/Virgo and NICER observations, together with examples of possible viable EoS relations (pink curves) based on Raaijmakers et al. (2021a). The black line indicates the EoS with the highest posterior support (the blue-shaded region indicates the posterior distribution). The green regions on the right plot indicate the multi-messenger constraints found from the NS event GW170817.

2.2. Waveform Model

The effect of high-frequency tidal disruptions on the GW amplitude of NSBH systems is usually modeled by introducing a cutoff frequency parameter that roughly indicates whether a merger is disruptive or not, and also marks the beginning of a possible disruption (Vallisneri 2000; Ferrari et al. 2009, 2010; Lackey et al. 2014; Pannarale et al. 2015a, 2015b). This is a distinctive feature of the waveform emitted by NSBH binaries: If the disruption, characterized by the cutoff frequency, takes

place before the NS crosses the BH's innermost-stable-circular orbit, then the ejected material from the NS can form a disk around the BH and suppress the amplitude of the waveform, leading to an accelerated merger with no post-merger GW signal. On the other hand, in the case of a nondisruptive merger (e.g., when the BH mass is very large), the waveform is shown to be comparable to binary BH waveforms (Pannarale et al. 2011), where, instead, the high-frequency amplitude is governed by the ringdown of the companion BH. Therefore, the difference between a BBH and a NSBH signal that is nondisruptive, is mainly in their GW phasing behavior.

To model the GW waveform, we use the Phenom-NSBH model (Thompson et al. 2020), which extends the analytical inspiral wave to incorporate the merger and post-merger dynamics through calibration with numerical relativity simulated waveforms. This waveform is built on the IMRPhenomC model for the amplitude and the IMRPhenomD model for the phasing, covering non-precessing systems with mass ratios ($Q = m_{\rm BH}/m_{\rm NS}$) from equal mass up to 15, BH spins aligned with the orbital angular momentum up to a dimensionless value of $|\chi_{\rm BH}| = 0.5$, and Λ ranging from 0 (the BBH limit) to 5000. However, it is important to note from (Thompson et al. 2020) (see Section III and Equation (6) therein) that the waveform's faithfulness in the $\chi_{\rm BH} < -0.4$ case is lower as compared to other parts of the parameter space (0.98 versus $\geqslant$0.99 elsewhere). Consequently, our results in this parameter region offer a representative comparison of disruptive versus nondisruptive effects. Yet, accuracy for anti-aligned spins might suffer due to limited waveform model testing, as indicated by Thompson et al. (2020), keeping in mind that for $\chi_{\rm BH} < 0$ cases, the model amplitude is only calibrated up to $Q < 4$ based on NR simulations.[7] In modeling the Phenom-NSBH waveform, the tidal corrections to the GW phase are incorporated as post-Newtonian (PN) spin-induced quadrupole corrections at 5 PN and 6 PN order (Hinderer et al. 2010; Vines et al. 2011). To first order, the change in GW phase scales linearly with Λ, through a dimensionless quantity defined as

$$\tilde{\Lambda} = \frac{48}{39}\frac{m_{{\rm NS},s}^4 (m_{{\rm NS},s} + 12 m_{{\rm BH},s})}{(m_{{\rm NS},s} + m_{{\rm BH},s})^5}\Lambda. \quad (2)$$

This scaling shows that finite-size effects are expected to be mainly detectable for NSBHs involving low-mass BHs. As the mass ratio increases, tidal effects scale away as Q^{-4} in the phase, making the nondisruptive NSBH signal hard to differentiate from a BBH signal. Therefore, in the case of short (≈less than 100 s) or low S/N (≈less than 30) signals, the only differences between these two waveform models—nondisruptive NSBH systems and BBH systems—could be the slightly different properties of the remnant quantities after the merger, which are hard to distinguish with the current GW detectors (Foucart et al. 2013a; Takami et al. 2014). Note that, in the case of possibly long and loud GW signals, the accumulated waveform phase difference between a BBH and a disruptive NSBH system (due to the presence of tidal terms in the latter case) can lead to bounds on Λ such that the BBH case ($\Lambda = 0$) gets excluded. However, the overall bounds on Λ for the nondisruptive systems are still expected to be broader than the disruptive ones, and generally uninformative in most of the cases.

For the GW amplitude in the Phenom-NSBH model, semi-analytical modeling of tidal effects at the late inspiral is adopted (Pannarale et al. 2015b). In this modeling, the merger of an NSBH binary is considered disruptive whenever the mass ratio $Q < Q_D(\mathcal{C}, \chi)$, with the threshold being fitted by

$$Q_D = \sum_{i,j=0}^{3} a_{i,j}\mathcal{C}^i\chi^j, \qquad i + j \leqslant 3, \quad (3)$$

where χ is the BH spin parameter and the fitting parameters $a_{i,j}$ are as given in Pannarale et al. (2015a). The corresponding fitted cutoff frequency $f_{\rm cut}$—which labels the starting point for considerable disruption in the merger—to this threshold is given by

$$f_{\rm cut} = \sum_{i,j,k=0}^{3} f_{\rm ijk}\,\mathcal{C}^i Q^j \chi^k, \qquad i + j + k \leqslant 3, \quad (4)$$

with the fitting parameters $f_{\rm ijk}$ (Pannarale et al. 2015a). The fitted threshold parameters depend on the EoS only implicitly and through the NS compactness. Moreover, the aforementioned waveform model approximates $\mathcal{C}$ in terms of Λ by using the quasi-universal relation on the compactness (Yagi & Yunes 2017):

$$\mathcal{C} = 0.371 - 0.0391\log(\Lambda_{\rm NS}) + 0.001056\log(\Lambda_{\rm NS})^2. \quad (5)$$

This allows us to quantify the disruptions of each merger solely based on the waveform parameters that can be derived from detected GW data.

Figure 2 shows a non-spinning NSBH GW characteristic signal $h_c = f \times |\tilde{h}(f)|$ at $z = 0.02$ (≈100 Mpc), for disruptive and nondisruptive mergers as compared to their BBH analog signal. For the disruptive mergers, the $f_{\rm cut}$ is also indicated and shows the approximate frequency at which the waveforms start to deviate from a BBH signal. As expected, increasing the mass ratio would change the mergers from being totally disruptive to nondisruptive. Although not shown here, we have also investigated that disruptive waveforms with a higher Λ have larger deviations from their BBH counterpart waveforms.[8]

2.3. Simulations and Sources

We simulate samples of individual NSBH binary events in the detector bands of the 3-interferometer ET and CE (i.e., 5 Hz to 4 kHz), and using a sampling frequency rate of 4096 Hz. For the possible CE sites, we choose the Northwestern USA and Southeastern Australia locations (see Gossan et al. (2022) for the detector coordinate details and further work). The ET site implemented in `lalsuite` (LIGO Scientific Collaboration 2018), and hence used in this work, is the same as the location of the Virgo detector. Having multiple detectors allows us to localize the GW sources and infer the different GW polarization content, thus allowing one to break the degeneracy between the luminosity distance and inclination angle for high S/N systems (Borhanian & Sathyaprakash 2022). Note that we are assuming that the calibration errors will be less than 1% in

[7] An alternative state-of-the-art model for NSBH mergers is based on the effective one-body approximation; see Matas et al. (2020).

[8] Note that the high-frequency amplitude increase of the BBH waveforms for the $Q = 4$, 6, 10 cases, as well as the mismatch with the dip in the BBH waveform, are due to the unphysical artifact in the waveform model and do not represent physical features (see also Figure 1 of Thompson et al. 2020).

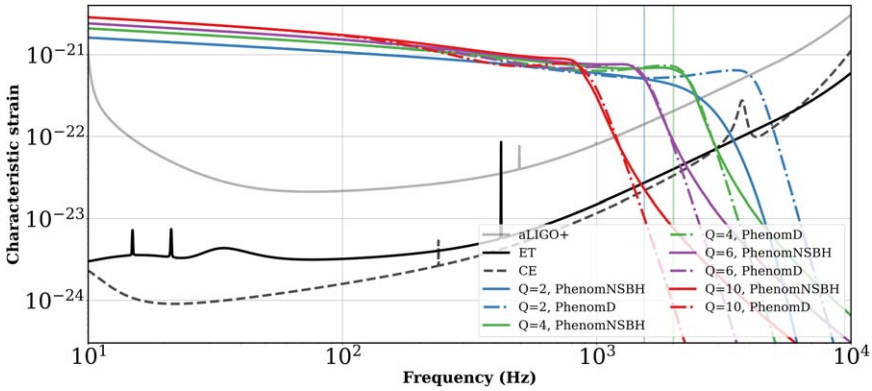

Figure 2. The dimensionless sensitivity curves $\sqrt{S_n \times f}$ and the characteristic signals $h_c = f \times |\tilde{h}(f)|$ as a function of frequency f. The solid lines correspond to the Phenom-NSBH model and the dotted–dashed lines to the corresponding BBH binary modeled signal IMRPhenomD for a system at $z = 0.02$ ($d_L \approx 100$ Mpc). As the mass ratio of the system increases, the mergers change from total disruption of the NS, with the amplitude of the waveform being exponentially suppressed at high frequencies, to nondisruptive NS for which the waveform is comparable to the BBH waveform. The shaded blue and green lines correspond to cutoff frequencies $f_{\rm cut}(Q = 2) = 1535$ Hz and $f_{\rm cut}(Q = 4) = 2000$ Hz.

the amplitude and phasing (see Huang et al. (2022) for a more detailed analysis).

For the injected cosmological parameters we use $H_0 = 67.4\,{\rm km\,s^{-1}\,Mpc^{-1}}$, along with the rest of the parameters as reported in Planck Collaboration et al. (2020). In order to isolate the effect of tidal interactions on the inference, as well as due to the limitations of the waveform model, we do not consider the effects of spin precession and orbital eccentricity here. The inclusion of spin precession, however, has been shown to improve the H_0 inference by breaking the distance-inclination degeneracy, in some NSBH systems (see Vitale & Chen (2018)).

We generate two sets of simulations:

(1) Set of individual mock binary samples that will allow us to compare the disruptive and nondisruptive mergers and their effect on the H_0 inference. We generate such mock binary samples, having fixed $m_{{\rm NS},s} = 1.4M_\odot$, $\Lambda = 490$. We vary the mass ratios to be $Q = m_{{\rm BH},d}/m_{{\rm NS},d} = \{2, 4, 6\}$, at a certain sky position and polarization of (R.A., decl., polarization) = (3.45, −0.41, 2.35) rad. In order to study the impact of GW parameters on the inference, we also choose the BH spins to be $\chi_{\rm BH} = \{0,\ 0.5,\ -0.5\}$ and consider systems with different inclination angles $\theta_{\rm jn}$ bracketing to the two extreme cases of edge-on and face-on binaries. Increasing the distance, as expected, would broaden the inferred bounds on Λ, as the disruptive binaries would merge outside the detector's sensitivity band. Here we consider binaries located at $z = 0.07$ and 0.2.

(2) Due to possible degeneracies between parameters and due to measurement uncertainties, the analysis of such single events may lead to multimodal H_0 measurements. To overcome these limitations, we also analyze the stacked catalog of mock binary samples of size $N = 10$, 70, and 100, in the ET+CE detector era. We distribute the binary systems uniformly in sky location, orientation, and volume ($\propto d_L^2$). We also sample from uniform distributions of BH and NS source masses and spins, the same as that of Section 2.4.1. For generating these samples, we also vary the initial choice of EoS parameter by uniformly sampling ≈3000 EoS choices based on the posterior distribution of Raaijmakers et al. (2021a). We consider the systems with the network S/N of above 8 to be detectable.

2.4. Statistical Framework

2.4.1. GW Parameter Inference

In order to perform a probabilistic inference of Λ and subsequently H_0 through Bayesian analysis (as described in, for example, Appendix B of Abbott et al. 2019b), we first evaluate the GW probability distribution function (PDF) $P(\theta_i|\boldsymbol{x})$ with $\boldsymbol{x}$ being the simulated GW strain observation and θ_i the set of waveform parameters that we want to estimate. For this, we marginalize the GW likelihood over the coalescence phase. We sample the marginal GW likelihood using the relative binning approach (Zackay et al. 2018), as implemented in the inference library `PyCBC` (Biwer et al. 2019) together with the `DYNESTY` nested sampler (Speagle 2020), using 2100–2500 live points. The relative binning method allows for fast analysis of GW signals by assuming that the difference between adequate waveforms in the frequency domain is describable by a smoothly varying perturbation. Having the fiducial gravitational waveforms close to where the likelihood peaks, this approach reduces the number of frequency points for the evaluation of the waveforms to $\mathcal{O}(10^2)$, as compared to $\mathcal{O}(10^7)$ for traditional GW parameter inference.

The prior choice on each parameter is as follows. We draw uniformly distributed BH masses from $P(m_{{\rm BH},s}) = U(2.5M_\odot, 12M_\odot)$ with the lower limit set in such a way as to allow BHs in the mass-gap region and the upper limit in such a way to avoid running into high values of Q for which the waveform approximation does not function. The NS masses are drawn from $P(m_{{\rm NS},s}) = U(1M_\odot, 2.5M_\odot)$, with the upper limit chosen to be above the current estimates of the maximum mass of NSs (Legred et al. 2021; Pang et al. 2021). We consider aligned-spin binary components with the dimensionless BH and NS spin parameter drawn from $P(\chi_{\rm BH}) = U(-0.5,\ 0.5)$ and the low-spin prior of $P(\chi_{\rm NS}) = U(-0.05,\ 0.05)$, respectively. Examining astrophysically motivated populations for NSBH mergers such as those in Broekgaarden et al. (2021) and Boersma & van Leeuwen (2022) is left for future work. The redshift parameter is sampled from $P(z) = U(0,\ 1.5)$. The inclination angle, sky position, phase, and polarization angles are isotropically distributed. The luminosity distance d_L is distributed uniformly in the comoving volume such that $P(d_L) \propto d_L^2$. For the EoS parameter, we choose a prior based on the multi-messenger constraints (as explained in

Section 2.1), covering up to 3000 viable EoS choices. Consequently, for each realization of the sampler, the Λ parameter is derived based on the sampled set of $\{z, m_{\mathrm{NS},d}, \mathrm{EoS}\}$ parameters, using the pycbc implemented transformation function `Lambda_from_multiple_tov_files`. For this, we require the sampling to be done in terms of z and $m_{\mathrm{NS},d}$ instead of Λ and $m_{\mathrm{NS},d}$. Moreover, in order to speed up the inference, we sample in detector-frame chirp mass and mass ratio instead of the individual masses.

2.4.2. Hubble Constant Inference

We estimate H_0 using a two-step Bayesian inference analysis. In order to estimate H_0 from the GW data, we use the redshift–distance relation as given by

$$d_L = \frac{c(1+z)}{H_0}\int_0^z \frac{dz'}{E(z')}, \tag{6}$$

where $E(z') = \sqrt{\Omega_r(1+z')^4 + \Omega_m(1+z')^3 + \Omega_{\mathrm{DE}}}$ corresponds to the assumption of a flat universe and Ω_r, Ω_m, and Ω_{DE} are the radiation, matter, and dark energy densities, respectively. In this analysis, we use the third-order Taylor expansion of Equation (6) around $z = 0$, i.e., for low redshifts.

Having the GW strain data $\boldsymbol{x}$ of a single event, the posterior on H_0 can be obtained from the semi- marginalized GW likelihood and the prior $P_0(H_0)$:

$$\frac{P(H_0|\boldsymbol{x})}{P_0(H_0)} = \int P(\boldsymbol{x}, \Lambda, d_L, m_{\mathrm{NS},d}|H_0)\,dd_L\,d\Lambda\,dm_{\mathrm{NS},d}, \tag{7}$$

where $P(\boldsymbol{x}, \Lambda, d_L, m_{\mathrm{NS},d}|H_0)$ is the GW likelihood marginalized over all the parameters other than $\{d_L, \Lambda, m_{\mathrm{NS},d}\}$. Equation (1) and Equation (6) allow us to write d_L as a function of cosmological parameters and the GW inferred parameters $\{\Lambda, m_{\mathrm{NS},d}\}$ such that $d_L = d_L(\Lambda, m_{\mathrm{NS},d}, H_0)$. The function `Lambda_from_multiple_tov_files` does the same for the Λ parameter, replacing it as a function of the sampling parameters $\{z, m_{\mathrm{NS},d}\}$. Therefore, the marginalized likelihood can be further expanded as

$$\begin{aligned}
&\int P(\boldsymbol{x}, \Lambda, d_L, m_{\mathrm{NS},d}|H_0)\,dd_L\,d\Lambda\,dm_{\mathrm{NS},d}\\
&= \int P(\boldsymbol{x}|\Lambda, m_{\mathrm{NS},d}, d_L)P(d_L|m_{\mathrm{NS},d}, \Lambda, H_0)\\
&\times P(\Lambda|m_{\mathrm{NS},d}, z) \times P_0(\Lambda, m_{\mathrm{NS},d}, d_L|H_0)\\
&\quad \times dd_L\,d\Lambda\,dm_{\mathrm{NS},d},
\end{aligned} \tag{8}$$

where again, P_0 shows the prior on each parameter. The constraint between parameters is defined through $P(d_L|m_{\mathrm{NS},d}, \Lambda, H_0)$ and $P(\Lambda|m_{\mathrm{NS},d}, z)$, and can be replaced by delta functions such that

$$\begin{aligned}
&\int P(\boldsymbol{x}, \Lambda, d_L, m_{\mathrm{NS},d}|H_0)\,dd_L\,d\Lambda\,dm_{\mathrm{NS}}\\
&= \int P(\boldsymbol{x}|\Lambda, m_{\mathrm{NS},d}, d_L)\delta(d_L - \hat{d}_L[m_{\mathrm{NS},d}, \Lambda, H_0])\\
&\quad \times \delta(\Lambda - \hat{\Lambda}[m_{\mathrm{NS},d}, z])P_0(\Lambda, m_{\mathrm{NS},d}, d_L|H_0)\\
&\quad \times dd_L\,d\Lambda\,dm_{\mathrm{NS},d}\\
&= P(\boldsymbol{x}|\hat{d}_L[m_{\mathrm{NS},d}\,z, H_0])P_0(H_0) = \mathcal{L}(H_0),
\end{aligned} \tag{9}$$

where in the last line we have applied the delta function and also marginalized over the rest of the parameters.

We perform the sampling of the semi-marginal likelihood $\mathcal{L}(H_0) = P(\boldsymbol{x}|\hat{d}_L[m_{\mathrm{NS},d}, z, H_0])$ using `pymultinest` (Buchner et al. 2014). In order to do so, we first perform a kernel density estimation fit to the semi-marginal likelihood using `kalepy` (Kelley 2021). We assume a flat prior on H_0 of the form $P_0(H_0) = U(10, 300)\,\mathrm{km\ s^{-1}\ Mpc^{-1}}$. In addition to this method, we also performed the direct sampling of H_0 through `pycbc` and recovered similar results, yet the two-step inference shows better convergence in some cases such as for low-redshift systems.

3. Results

3.1. Single Events: Λ Detectability

It is widely expected that disruptive NSBH mergers, once visible in a detector band, will allow for more accurate measurement of the NS tidal effects, and hence, the redshift. In order to quantify the effect of high-frequency tidal disruption on the parameter inference, we analyze a selected sample of single NSBH events with different Q and χ_{BH}. During the inference, the EoS parameter is varied freely, with a prior consistent with the posterior distribution found in Raaijmakers et al. (2021a) (see Section 2).

The derived constraints on the Λ parameter are shown in Figure 3, for systems with $z = 0.07$ (top, $d_L \approx 300$ Mpc) and $z = 0.2$ (bottom, $d_L \approx 1$ Gpc). All the systems that are located at $z = 0.07$ merge within the ET+CE detector's bandwidth. The network S/Ns for the top panel are ≈367, 470, and 541, and for the bottom panel are ≈107, 138, and 159 for the $Q = 2$, 4, and 6, respectively. The initial inclination angle is chosen as $\theta_{\mathrm{ij}} = 90°$ for these plots. Due to the high S/N of the selected events, we have shown that the results remain consistent once changing θ_{ij} with only minor variations in the inference of this parameter, which is expected given that the redshift (and hence Λ) is primarily inferred from the phasing of waveforms. Note however that, the change in θ_{ij} affects the inference of d_L that enters the GW amplitude. This has been shown in multiple studies such as those of Hinderer et al. (2010) and Nissanke et al. (2010, 2013a), and specifically for the inference of H_0 with dark binary NSs in Chatterjee et al. (2021). For systems at lower S/N we should however expect to see the effect of θ_{ij} on the inference of d_L, and consequently H_0.

Focusing on the non-spinning cases considered here, we see that, the disruptive mergers ($Q = 2$) constrain Λ (95% credible interval) to $\Lambda = 570^{+216}_{-195}$ (top) and $\Lambda = 578^{+635}_{-516}$ (bottom), with the relative error of ≈16% in both cases. In the case of highly nondisruptive mergers ($Q = 6$), these values worsen and are given as $\Lambda = 868^{+420}_{-460}$ (top) and $\Lambda = 1549^{+1284}_{-1223}$ (bottom), with a relative error of ≈77% in the former case, and an uninformative constraint on the latter case. This analysis does not clearly show the expected positive (negative) effect of prograde (retrograde) BH spin on the inference of Λ. Possible sources of limitations can be the degeneracies (such as the degeneracy between the reduced mass, entering at 1 PN order, and the spin, entering at 1.5 PN order (Cutler & Flanagan 1994), as well as the limitation of Phenom_NSBH model at prograde spins: we anticipate that a more detailed analysis of the BH spin effects on Λ inference is not feasible with the current limitations of the GW waveform models.

In general, having a flat prior on Λ, exclusion of $\Lambda = 0$ value from the posterior samples would suggest that GW information alone can distinguish NSBH systems from a BBH merger. This may happen if a merger happens in-band for a detector system,

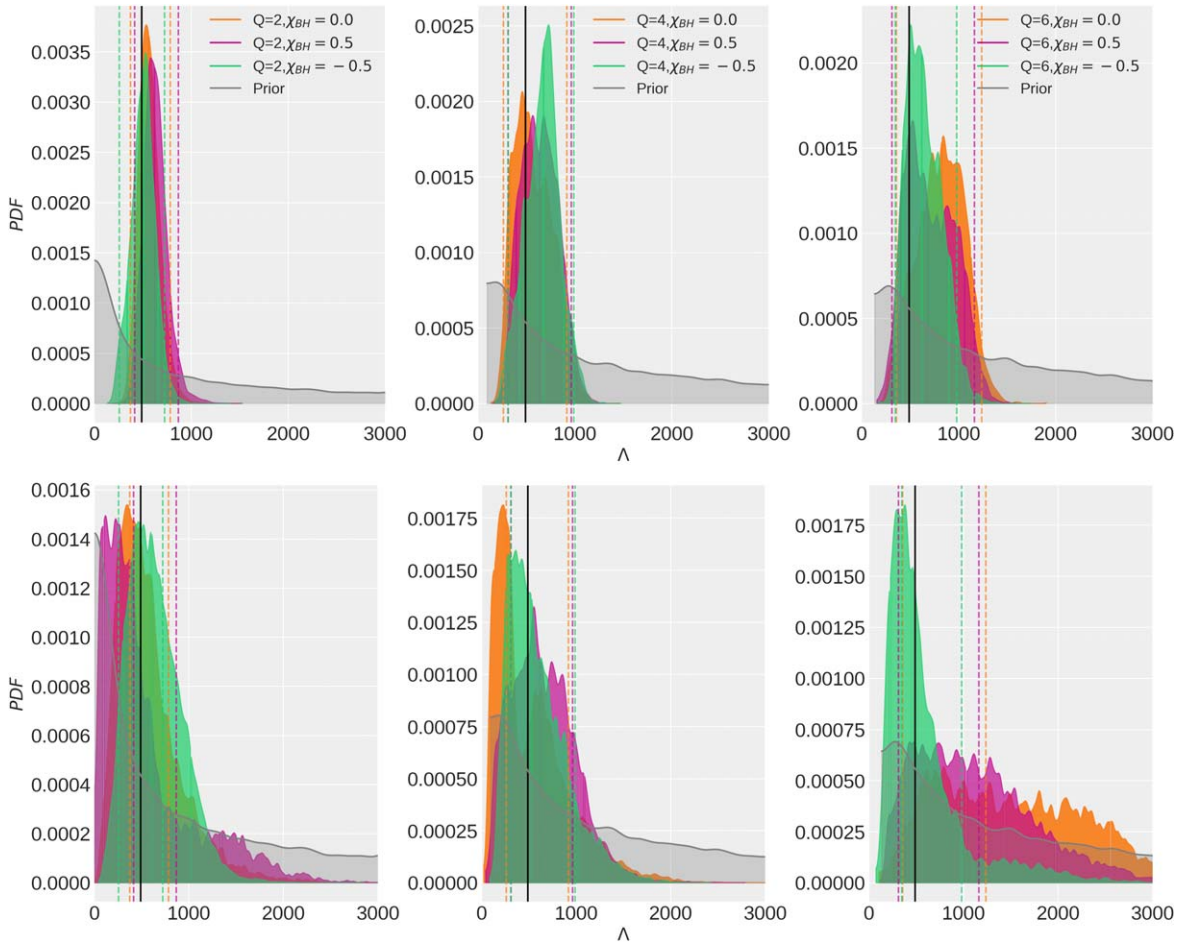

Figure 3. The posterior probability density and the 90% credible regions of Λ parameter as measured for $Q = 2$ (disruptive), $Q = 4$ (mildly disruptive), and $Q = 6$ (nondisruptive) systems located at $z = 0.07$ (top) and $z = 0.2$ (bottom). The orange, pink, and green shaded regions correspond to the choice of $\chi_{\rm BH} = 0$, $\chi_{\rm BH} = 0.5$, and $\chi_{\rm BH} = -0.5$, respectively. The black vertical lines correspond to the injected value of $\Lambda = 490$ and the gray-shaded regions show the implied prior on the Λ parameter.

or by having a long detected signal duration for an event: over a long inspiral time, the BBH and nondisruptive NSBH signals can get a dephasing of $\approx\mathcal{O}(1)$ rad from the point-particle tidal effects, which makes the waveforms nonidentical. However, it is important to keep in mind that, in our analysis, the inferred bounds also depend on the $\{m_{\rm NS}, z, \rm EoS\}$ priors, which may a priori exclude the $\Lambda = 0$ value. More specifically, the `Lambda_from_multiple_tov_files` function assigns a $\Lambda = 0$ value to each sampled $m_{{\rm NS},s}$ that exceeds the maximum allowed NS physical mass for a given EoS parameter file, and hence allows for some of the systems to be predicted as BBH systems. This implied prior on Λ is shown in the gray-shaded regions of Figure 2. For the middle and right panels, the minimum allowed Λ values of the prior are 91 and 132, respectively. In the cases where $\Lambda = 0$ is allowed by the implied prior on Λ (left panels), the exclusion of this value from the posterior samples would suggest that GW information alone can distinguish this system from a BBH merger, which is critical for the validity of this approach on real GW data. This can be seen in the top left panel of Figure 2 but not in the bottom left panel, due to the lower S/Ns of the latter systems.

3.2. Single Events: Pair Plots and Statistical Uncertainties

In order to see the degeneracy between sampled GW parameters and their effect on the overall inference, we have shown the full inference results for two of the considered examples, including the bounds on H_0 from these single events in Figures 4 and 5. In this section, we show the results of the method of direct sampling of H_0, instead of the post-processing approach. This is necessary if we want to capture the degeneracy between the Λ, z, and H_0 parameters all in one plot. We confirm that both of the methods result in similar constraints on the parameters. Here we have chosen $\theta_{\rm ij} = 30$ given that it represents a probable angle for most of the future binary observations.

Our results for the inference of the redshift parameter are comparable with the similar bounds found by studying single BNS systems at $z < 1$ (Messenger & Read 2012). However, while Messenger & Read (2012) considered a $Q = 1$, $m_{{\rm NS},s} = 1.4 M_{\odot}$ BNS case, such a system does not represent a physical NSBH binary and hence we cannot perform a one-to-one comparison with the results of Messenger & Read (2012).

We note that, even for highly disruptive systems, the measurement of H_0 by individual events is affected by covariances between the parameters that result in low precision, as well as hidden systematic uncertainties. This can be seen, for instance, for the low-redshift points shown in Figure 6, where the error on H_0 inference is following the trend of z error, rather than being small. Also, as shown in Figure 6, we can clearly see that the ability to constrain H_0 from single events is limited

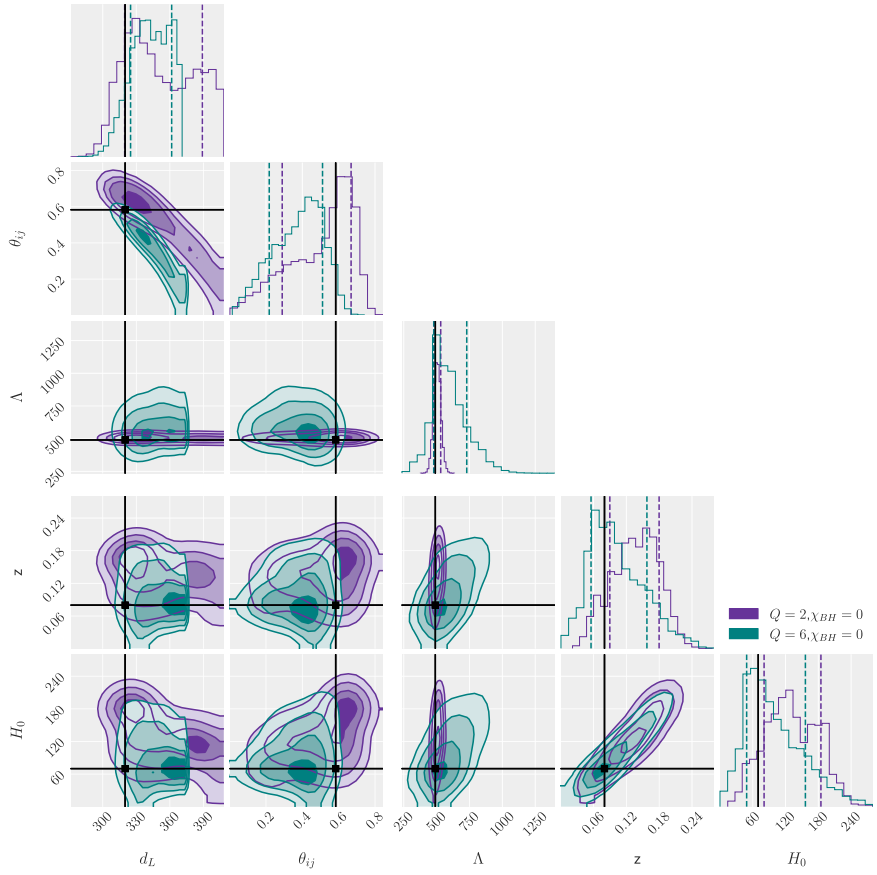

Figure 4. (Single runs) The posterior probability density and the 68% credible intervals of $\{d_L, \theta_{ij}, \Lambda, z, H_0\}$ as measured for the $Q = 2$ (purple) and $Q = 6$ (green) systems located at $z = 0.07$ with $\theta_{ij} = 30$. The plot shows the results of direct sampling.

at high distances and saturates at a certain error limit. This follows from the limitation on the inference of z, which is mainly tied to the uncertainties in inferring Λ, as well as d_L. Overall, we see a decrease in the fractional error, since the source frame high-frequency part of the signal is redshifted and appears in the sensitive part of the detectors. A similar analysis in Chatterjee et al. (2021) as well as in Ghosh et al. (2022) shows the same limitations on the H_0 inference at high distances, for the case of BNS systems, even though the modeling approaches are different from what we consider. Although not shown here, we have also found that fixing the choice of the EoS parameter does not significantly improve the fractional error estimates of H_0 and redshift at high distances.

Overall, in the case of multiple events, the statistical uncertainty is expected to decrease as the inverse square root of the number of events yet this does not affect the systematic uncertainties and general limitations. We note again that, we have assumed that calibration errors will be negligible in the next-generation GW detectors, yet this assumption should be revised in future works.

3.3. Stacked Events: H_0 Detectability

The next-generation detectors, such as CE and ET, are expected to detect tens of thousands of NSBH events per year and hence can provide a precise statistical measurement of H_0. Here we stack the individual H_0 measurements of simulated synthetic NSBH mergers as described in Section 2.3. The combined H_0 PDF is found by multiplying the single PDFs of Equation (7) such that

$$P(H_0|\{\boldsymbol{x}_1,\ldots\boldsymbol{x}_N\}) = \prod_{i=1}^{N} P(H_0|\boldsymbol{x}_i) = P_0(H_0)\mathcal{L}_i(H_0), \qquad (10)$$

where we use an overall flat prior $P(H_0)$ on the stacked H_0 to get the stacked PDF.

The results are shown in Figure 7 for the different catalogs considered. The gray-dashed lines show the individual PDFs and the green line shows the stacked PDF, which is peaked at the injected H_0 value. We find that having $N = 10$, 50, and 100, the H_0 can be measured with a precision of ≈13%, 6.6%, and 4% (at the 68% credible interval). This precision is in agreement with the $\sqrt{N}$ scaling of the relative errors, which can be used as a first-order estimate for uncertainties in a catalog of events (see Hinderer et al. 2010).

We note that, in all the catalogs considered, the nondisruptive NSBH systems are the most dominant as they naturally cover a broader range of the parameter space once we generate the population parameters uniformly. This may not necessarily be the case for more realistic population models of NSBH systems (see Mapelli et al. 2019; Broekgaarden et al. 2021). If a population allows for more disruptive mergers (or if we end up detecting more of these systems) (Mapelli & Giacobbo 2018), we would naturally expect more stringent constraints on Λ-related parameters. Also, note that we are not incorporating any GW detector selection effects in this analysis (see Abbott et al. 2019a; Gerosa et al. 2020), and references therein, for possible methods of including the selection biases.)

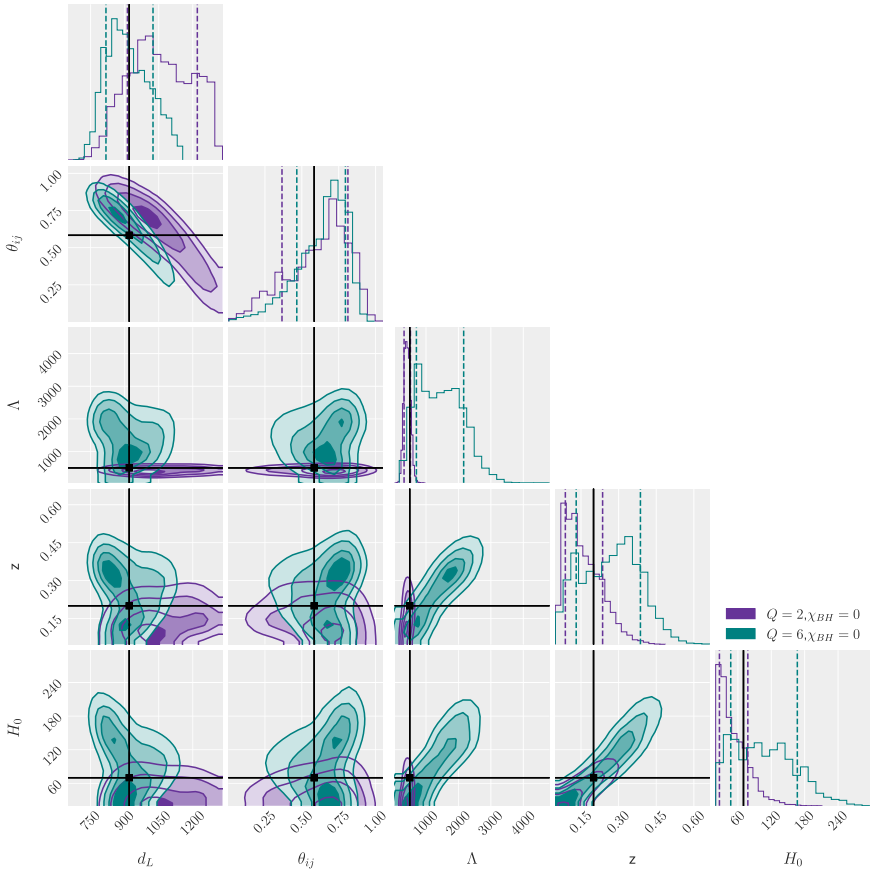

Figure 5. (Single runs) The posterior probability density and the 68% credible intervals of $\{d_L, \theta_{ij}, \Lambda, z, H_0\}$ as measured for the $Q = 2$ (purple) and $Q = 6$ (green) systems located at $z = 0.2$ and $\theta_{ij} = 30$. The plot shows the results of direct sampling.

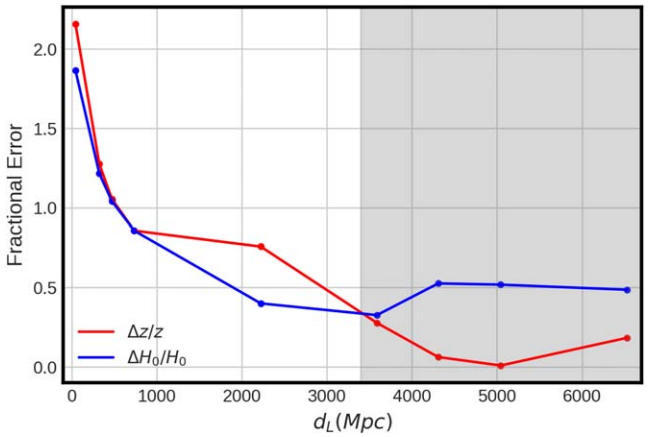

Figure 6. The fractional statistical error of z (red) and H_0 (blue) as a function of d_L for a subset of runs with $Q = 2$. The injected parameters are the same as those of Section 2.3. The gray-shaded region shows the threshold of SN = 30.

Our results for $N = 100$ case show the same order of inference precision to that of a similar study performed on BNS mergers in the CE detector era (Chatterjee et al. 2021). There the authors report a 2% precision in the measurement of H_0 with $N = \mathcal{O}(10^3)$ BNS events as seen by one CE detector, using the universal binary-Love relations to model Λ.

4. Conclusions

We have analyzed the prospects of inferring H_0 from the GW data of NSBH events without considering EM counterparts, based on the foundational idea that the presence of matter terms in GWs breaks the degeneracy between the mass parameters and redshift, allowing simultaneous measurement of both the luminosity distance and redshift (Messenger & Read 2012). In this paper, we model the NS tidal parameter based on the latest multi-messenger constraints on NS matter from NICER + LIGO/Virgo/KAGRA, hence, modeling the Λ parameter solely based on empirically determined viable EoS. Note though that systematic biases might be introduced through the specific choice of high-density EoS parameterization, but we will leave the effect of this on the H_0 measurement to future work. Our analysis is done on both single NSBH systems, as well as their synthetic catalogs, in the ET+CE detector era.

The unique merger phenomenology of NSBH systems allows for highly disruptive events that are key candidates for the precise measurement of NS tidal parameters, once they merge within the sensitivity band of the GW detectors considered. In the case of single events, by comparing some examples of disruptive and nondisruptive mergers, we show that in-band mergers of disruptive systems can constrain Λ with $\approx$36% precision, while this number increases to $\approx$50% for the in-band mergers of nondisruptive systems. In the case of a system merging outside the detector's sensitivity bound, the disruptive mergers result in a mostly uninformative precision of $\approx$95% and the nondisruptive mergers lead to totally uninformative constraints on Λ. Note, however, that the values of these ranges are highly dependent on the specific initial signal configurations and may change by comparing signals with, e.g., different duration, distance, inclination, or sky location.

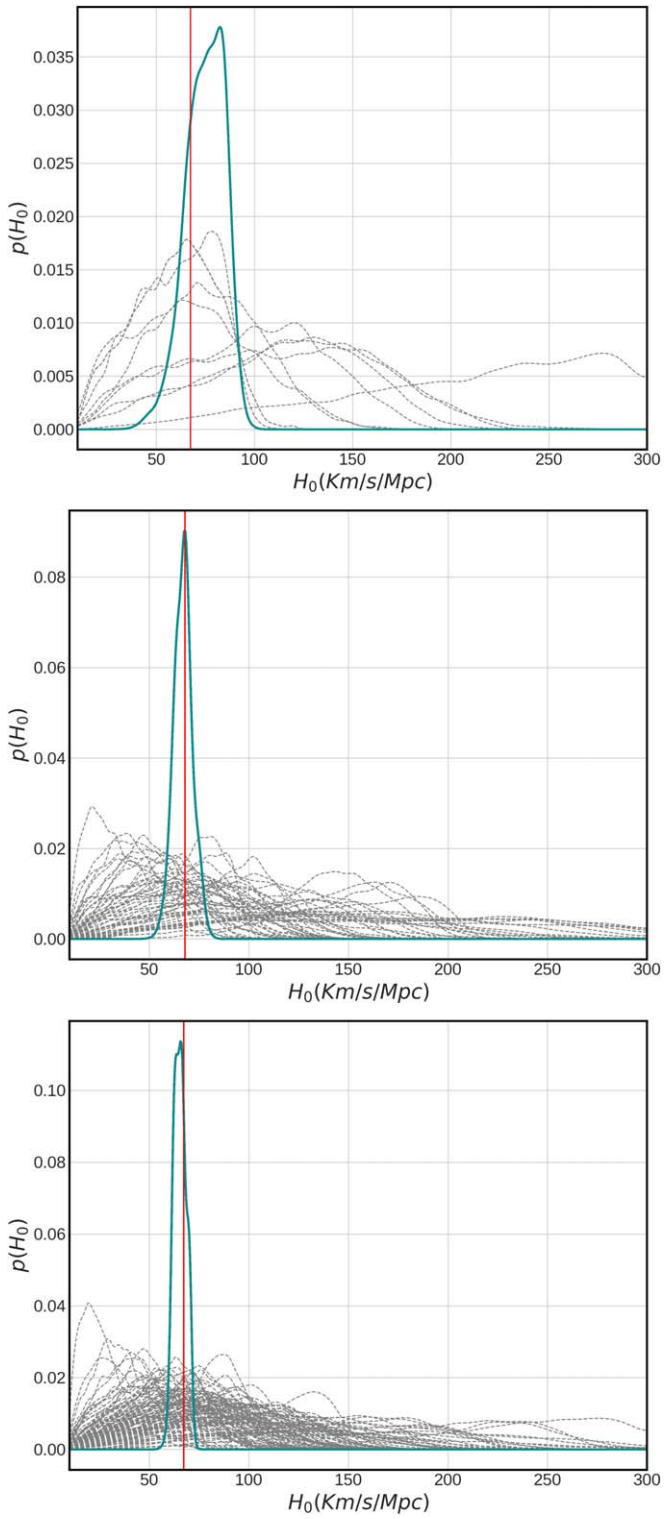

Figure 7. The single and stacked H_0 PDFs for simulated NSBH mergers in the ET+CE detector era with $N = 10$, 50, and 100 simulated events. The vertical line corresponds to the true value of $H_0 = 67.4$ km s^{-1} Mpc^{-1}. The estimated precision on H_0 are ≈13%, 6.6%, and 4% for the $N = 10$, 50, and 100 cases, respectively.

The overall improvement in H_0 inference is, however, limited due to the fundamental degeneracy between the redshift and H_0 parameter. Importantly, we find that the precision at which the redshift can be inferred with this approach is not strong enough to result in unbiased and highly constrained measurements of H_0 from single events. This retains the need for accurate localization of systems in order to have a highly accurate redshift (and H_0) estimation. Also, we realize that the measurement of the redshift (and hence the H_0) with this approach is strongly affected by the details of spin precession and tidal distortion modeling in GW waveforms, highlighting the need for improved GW template models of NSBH mergers.

In order to improve against this fundamental limitation of H_0 inference, we analyze synthetic sets of NSBH GW signals with samples of $N = 10$, 50, and 100 events, with the population being generated by uniform sampling of all parameters. Our results show that for the ET + CS detector era, this method can result in unbiased 13%–4% precision in the measurement of H_0, once the same waveform model is used for the injection and recovery of the signals.

Future detailed analysis following this work can be done by including the effect of orbital precession in the analyzed signals. This is important as systems with large retrograde BH spins can result in significant orbital precession. We also note that, due to the intrinsic limitation of the waveform model Phenom-NSBH to $m_{\mathrm{NS},d} \ll 3M_{\odot}$, the detectable NS population depends on the redshift of the event. This modeling results in NSs with high masses being less dominant at high redshifts and also that the lightest NSs (i.e., $m_{\mathrm{NS},s} \approx 1M_{\odot}$) cannot be located at redshifts higher than $z = 2$, which is a serious limiting factor in the analysis of these events in the next-generation detector era. Also, including higher than quadrupole multipole moments in the waveform modeling is shown to be necessary for precise parameter measurements for systems with $Q > 3$ (Kalaghatgi et al. 2020). Another important avenue of improvement is to study more realistic NSBH population models. In principle, population models predicting a greater number of disruptive mergers would result in more stringent constraints on H_0.

Acknowledgments

We thank Stephen Feeney, Daniel Mortlock, Uddipta Bhardwaj, and Suvodip Mukherjee for useful discussions and suggestions, and Archisman Gosh for comments on the manuscript. B.S., G.R., and S.M.N. are grateful for the financial support from the Nederlandse Organisatie voor Wetenschappelijk Onderzoek (NWO) through the Projectruimte and VIDI grants (Nissanke). T.H. and S.M.N. also acknowledge financial support from the NWO sector plan. F.F. gratefully acknowledges support from the DOE through grant DE-SC0020435, and from NASA through grants 80NSSC18K0565 and 80NSSC22K0719. A.R.W gratefully acknowledges support from the STFC through grant ST/S000550/1.

ORCID iDs

Banafsheh Shiralilou https://orcid.org/0000-0003-1604-9805
Geert Raaiijmakers https://orcid.org/0000-0002-9397-786X
Bastien Duboeuf https://orcid.org/0000-0002-9542-3852
Samaya Nissanke https://orcid.org/0000-0001-6573-7773
Francois Foucart https://orcid.org/0000-0003-4617-4738
Tanja Hinderer https://orcid.org/0000-0002-3394-6105
Andrew R. Williamson https://orcid.org/0000-0002-7627-8688

References

Abbott, B. P., Abbott, R., Abbott, T. D., et al. 2017a, ApJL, 848, L13
Abbott, B. P., Abbott, R., Abbott, T. D., et al. 2017b, Natur, 551, 85

Abbott, B. P., Abbott, R., Abbott, T. D., et al. 2019a, ApJL, 882, L24
Abbott, B. P., Abbott, R., Abbott, T. D., et al. 2019b, PhRvX, 9, 031040
Abbott, R., Abbott, T. D., Abraham, S., et al. 2021, ApJL, 915, L5
Abbott, R., Abe, H., Acernese, F., et al. 2023, ApJ, 949, 76
Planck Collaboration, Aghanim, N., Akrami, Y., et al. 2020, A&A, 641, A6
Al-Mamun, M., Steiner, A. W., Nättilä, J., et al. 2021, PhRvL, 126, 061101
Biwer, C. M., Capano, C. D., De, S., et al. 2019, PASP, 131, 024503
Boersma, O. M., & van Leeuwen, J. 2022, A&A, 664, A160
Borhanian, S., Dhani, A., Gupta, A., Arun, K. G., & Sathyaprakash, B. S. 2020, arXiv:2007.02883
Borhanian, S., & Sathyaprakash, B. S. 2022, arXiv:2202.11048
Brege, W., Duez, M. D., Foucart, F., et al. 2018, PhRvD, 98, 063009
Broekgaarden, F. S., Berger, E., Neijssel, C. J., et al. 2021, MNRAS, 508, 5028
Buchner, J., Georgakakis, A., Nandra, K., et al. 2014, A&A, 564, A125
Capano, C. D., Tews, I., Brown, S. M., et al. 2020, NatAs, 4, 625
Chase, E. A., O'Connor, B., Fryer, C. L., et al. 2022, ApJ, 927, 163
Chatterjee, D., Hegade, K. R. A., Holder, G., et al. 2021, PhRvD, 104, 083528
Chen, H.-Y., Fishbach, M., & Holz, D. E. 2018, Natur, 562, 545
Chen, H.-Y., Haster, C.-J., Vitale, S., Farr, W. M., & Isi, M. 2022, MNRAS, 513, 2152
Cigarrán Díaz, C., & Mukherjee, S. 2022, MNRAS, 511, 2782
Cutler, C., & Flanagan, É. E. 1994, PhRvD, 49, 2658
Dalal, N., Holz, D. E., Hughes, S. A., & Jain, B. 2006, PhRvD, 74, 063006
Deaton, M. B., Duez, M. D., Foucart, F., et al. 2013, ApJ, 776, 47
Del Pozzo, W., Li, T. G. F., & Messenger, C. 2017, PhRvD, 95, 043502
Dietrich, T., Coughlin, M. W., Pang, P. T. H., et al. 2020, Sci, 370, 1450
Doneva, D. D., & Pappas, G. 2018, The Physics and Astrophysics of Neutron Stars, Astrophysics and Space Science Library, Vol. 457 (Cham: Springer), 737
Essick, R., Landry, P., & Holz, D. E. 2020, PhRvD, 101, 063007
Etienne, Z. B., Liu, Y. T., Shapiro, S. L., & Baumgarte, T. W. 2009, PhRvD, 79, 044024
Evans, M., Adhikari, R. X., Afle, C., et al. 2021, arXiv:2109.09882
Farr, W. M., Fishbach, M., Ye, J., & Holz, D. E. 2019, ApJL, 883, L42
Feeney, S. M., Peiris, H. V., Nissanke, S. M., & Mortlock, D. J. 2021, PhRvL, 126, 171102
Feeney, S. M., Peiris, H. V., Williamson, A. R., et al. 2019, PhRvL, 122, 061105
Ferrari, V., Gualtieri, L., & Pannarale, F. 2009, CQGra, 26, 125004
Ferrari, V., Gualtieri, L., & Pannarale, F. 2010, PhRvD, 81, 064026
Fishbach, M., Gray, R., Magaña Hernandez, I., et al. 2019, ApJL, 871, L13
Flanagan, E. E. 1998, PhRvD, 58, 124030
Foucart, F. 2012, PhRvD, 86, 124007
Foucart, F. 2020, FrASS, 7, 46
Foucart, F., Buchman, L., Duez, M. D., et al. 2013a, PhRvD, 88, 064017
Foucart, F., Deaton, M. B., Duez, M. D., et al. 2013b, PhRvD, 87, 084006
Foucart, F., Duez, M. D., Hinderer, T., et al. 2019a, PhRvD, 99, 044008
Foucart, F., Duez, M. D., Kidder, L. E., et al. 2019b, PhRvD, 99, 103025
Gayathri, V., Healy, J., Lange, J., et al. 2020, arXiv:2009.14247
Gendreau, K. C., Arzoumanian, Z., Adkins, P. W., et al. 2016, Proc. SPIE, 9905, 99051H
Gerosa, D., Pratten, G., & Vecchio, A. 2020, PhRvD, 102, 103020
Ghosh, T., Biswas, B., & Bose, S. 2022, PhRvD, 106, 123529
Gossan, S. E., Hall, E. D., & Nissanke, S. M. 2022, ApJ, 926, 231
Gray, R., Messenger, C., & Veitch, J. 2022, MNRAS, 512, 1127
Greif, S. K., Raaijmakers, G., Hebeler, K., Schwenk, A., & Watts, A. L. 2019, MNRAS, 485, 5363
Guerra Chaves, A., & Hinderer, T. 2019, JPhG, 46, 123002
Hebeler, K., Lattimer, J. M., Pethick, C. J., & Schwenk, A. 2013, ApJ, 773, 11
Hinderer, T., Lackey, B. D., Lang, R. N., & Read, J. S. 2010, PhRvD, 81, 123016
Holz, D. E., & Hughes, S. A. 2005, ApJ, 629, 15
Hotokezaka, K., Nakar, E., Gottlieb, O., et al. 2019, NatAs, 3, 940
Huang, Y., Chen, H.-Y., Haster, C.-J., et al. 2022, arXiv:2204.03614
Hubble, E. 1929, PNAS, 15, 168
Huth, S., Pang, P. T. H., Tews, I., et al. 2022, Natur, 606, 276
Kalaghatgi, C., Hannam, M., & Raymond, V. 2020, PhRvD, 101, 103004
Kelley, L. Z. 2021, JOSS, 6, 2784
Lackey, B. D., Kyutoku, K., Shibata, M., Brady, P. R., & Friedman, J. L. 2014, PhRvD, 89, 043009
Landry, P., & Essick, R. 2019, PhRvD, 99, 084049
Landry, P., Essick, R., & Chatziioannou, K. 2020, PhRvD, 101, 123007
Lattimer, J. M., & Schramm, D. N. 1974, ApJL, 192, L145
Legred, I., Chatziioannou, K., Essick, R., Han, S., & Landry, P. 2021, PhRvD, 104, 063003
LIGO Scientific Collaboration 2018, LSC Algorithm Library Suite, lalsuite Project ID: 1438 doi:10.7935/GT1W-FZ16
LIGO Scientific Collaboration, Virgo Collaboration, KAGRA Collaboration, et al. 2021, arXiv:2111.03606
Lindblom, L. 2018, PhRvD, 97, 123019
Maggiore, M., Van Den Broeck, C., Bartolo, N., et al. 2020, JCAP, 2020, 050
Mapelli, M., & Giacobbo, N. 2018, MNRAS, 479, 4391
Mapelli, M., Giacobbo, N., Santoliquido, F., & Artale, M. C. 2019, MNRAS, 487, 2
Matas, A., Dietrich, T., Buonanno, A., et al. 2020, PhRvD, 102, 043023
Messenger, C., & Read, J. 2012, PhRvL, 108, 091101
Metzger, B. D., & Berger, E. 2012, ApJ, 746, 48
Miller, M. C., Lamb, F. K., Dittmann, A. J., et al. 2019, ApJL, 887, L24
Miller, M. C., Lamb, F. K., Dittmann, A. J., et al. 2021, ApJL, 918, L28
Mortlock, D. J., Feeney, S. M., Peiris, H. V., Williamson, A. R., & Nissanke, S. M. 2019, PhRvD, 100, 103523
Mukherjee, S., Ghosh, A., Graham, M. J., et al. 2020, arXiv:2009.14199
Mukherjee, S., Krolewski, A., Wandelt, B. D., & Silk, J. 2022, arXiv:2203.03643
Mukherjee, S., Lavaux, G., Bouchet, F. R., et al. 2021a, A&A, 646, A65
Mukherjee, S., Wandelt, B. D., Nissanke, S. M., & Silvestri, A. 2021b, PhRvD, 103, 043520
Nicolaou, C., Lahav, O., Lemos, P., Hartley, W., & Braden, J. 2020, MNRAS, 495, 90
Nissanke, S., Holz, D. E., Dalal, N., et al. 2013a, arXiv:1307.2638
Nissanke, S., Kasliwal, M., & Georgieva, A. 2013b, ApJ, 767, 124
Nissanke, S., Holz, D. E., Hughes, S. A., Dalal, N., & Sievers, J. L. 2010, ApJ, 725, 496
O'Boyle, M. F., Markakis, C., Stergioulas, N., & Read, J. S. 2020, PhRvD, 102, 083027
Oguri, M. 2016, PhRvD, 93, 083511
Palmese, A., deVicente, J., Pereira, M. E. S., et al. 2020, ApJL, 900, L33
Pang, P. T. H., Tews, I., Coughlin, M. W., et al. 2021, ApJ, 922, 14
Pannarale, F., Berti, E., Kyutoku, K., Lackey, B. D., & Shibata, M. 2015a, PhRvD, 92, 081504
Pannarale, F., Berti, E., Kyutoku, K., Lackey, B. D., & Shibata, M. 2015b, PhRvD, 92, 084050
Pannarale, F., Rezzolla, L., Ohme, F., & Read, J. S. 2011, PhRvD, 84, 104017
Raaijmakers, G., Greif, S. K., Hebeler, K., et al. 2021a, ApJL, 918, L29
Raaijmakers, G., Nissanke, S., Foucart, F., et al. 2021b, ApJ, 922, 269
Reitze, D., Adhikari, R. X., Ballmer, S., et al. 2019, BAAS, 51, 35
Riess, A. G., Yuan, W., Macri, L. M., et al. 2021, ApJL, 934, L7
Riley, T. E., Watts, A. L., Bogdanov, S., et al. 2019, ApJL, 887, L21
Riley, T. E., Watts, A. L., Ray, P. S., et al. 2021, ApJL, 918, L27
Sathyaprakash, B., Bailes, M., Kasliwal, M. M., et al. 2019, BAAS, 51, 276
Schutz, B. F. 1986, Natur, 323, 310
Seto, N., & Kyutoku, K. 2018, MNRAS, 475, 4133
Shibata, M., Kyutoku, K., Yamamoto, T., & Taniguchi, K. 2009, PhRvD, 79, 044030
Soares-Santos, M., Palmese, A., Hartley, W., et al. 2019, ApJL, 876, L7
Speagle, J. S. 2020, MNRAS, 493, 3132
Stephens, B. C., East, W. E., & Pretorius, F. 2011, ApJL, 737, L5
Takami, K., Rezzolla, L., & Baiotti, L. 2014, PhRvL, 113, 091104
Taylor, S. R., Gair, J. R., & Mandel, I. 2012, PhRvD, 85, 023535
Thompson, J. E., Fauchon-Jones, E., Khan, S., et al. 2020, PhRvD, 101, 124059
Vallisneri, M. 2000, PhRvL, 84, 3519
Vasylyev, S., & Filippenko, A. 2020, ApJ, 902, 149
Vines, J., Flanagan, E. E., & Hinderer, T. 2011, PhRvD, 83, 084051
Vitale, S., & Chen, H.-Y. 2018, PhRvL, 121, 021303
Yagi, K., & Yunes, N. 2017, PhR, 681, 1
Zackay, B., Dai, L., & Venumadhav, T. 2018, arXiv:1806.08792